Helium-assisted, solvent-free electro-activation of 3D printed conductive carbon-polylactide electrodes by pulsed laser ablation

Maciej J. Glowacki[1,#], Mateusz Cieslik[1,#], Miroslaw Sawczak[2], Adrian Koterwa[3],

Iwona Kaczmarzyk[1], Rafal Jendrzejewski[2], Lukasz Szynkiewicz[1], Tadeusz Ossowski[3],

Robert Bogdanowicz[1], Pawel Niedzialkowski[3], Jacek Ryl[1,*]

[1] Gdansk University of Technology, Narutowicza 11/12, 80-233 Gdansk, Poland

[2] The Szewalski Institute of Fluid-Flow Machinery, Polish Academy of Sciences, Fiszera 14, 80-231 Gdansk, Poland

[3] Department of Analytical Chemistry, University of Gdansk, Wita Stwosza 63, Gdansk 80-308, Poland

[*] Correspondence: Jacek Ryl – jacek.ryl@pg.edu.pl

[#] these authors contributed equally to the manuscript

Abstract

Fused filament fabrication is one of the most rapidly developing 3D printing techniques, with numerous applications, including in the field of applied electrochemistry. Here, the utilisation of conductive carbon black polylactic acid (CB-PLA) for 3D printouts is the most promising. To use CB-PLA as an electrode material, an activation process must be performed, removing the polymer matrix and uncovering the electrically conductive filler. We present a novel, alternative approach towards CB-PLA activation with Nd:YAG (λ = 1064 nm) laser ablation. We present and discuss the activation efficiency based on various laser source operating conditions, and the gas matrix. The XPS, contact angle, and Raman analyses were performed for evaluation of the surface chemistry and to discuss the mechanism of the activation process. The ablation process carried out in an inert gas matrix (helium) delivers a relatively high electrochemically active surface area of the CB-PLA electrode, while the resultant charge transfer process is hindered when activated in the air plausibly due to the formation of thermally induced oxide layers. The electroanalytical performance of laser-treated CB-PLA in a He atmosphere was confirmed through caffeine detection, offering detection limits of 0.49 and 0.40 μM (S/N = 3) based on CV and DPV studies, respectively.

1. Introduction

3D printing technologies have found application in diverse branches of industry, such as industrial design, automobiles, architecture, mechanical engineering, biomedical engineering, etc. At present, researchers are exploring new materials, which extend the potential application of 3D printing [1–3]. The most popular 3D printing technology is fused filament fabrication (FFF), where thermoplastic materials are used as filaments and the object is printed layer-by-layer. FFF technology is also the most accessible, due to its relatively low costs of purchase and operation, ease of use, and the largest selection of materials for printing, including biodegradable polylactic acid (PLA) and its composites. The high conductivity of PLA composites is most often achieved through the utilisation of various electrically conductive carbon fillers, such as graphene or carbon black (CB). Carbon black (CB) is a very attractive material due to its high conductivity, biocompatibility, and chemical inertness [4], while its main advantage compared to other carbonaceous nanomaterials is its low cost. Due to this fact, CB is the most common electrically conductive additive used in batteries, capacitors, and supercapacitors [5–7], and also printable inks and FFF 3D printable polymers, as used in this case. Possessing higher catalytic activity than highly oriented graphite or carbon nanotubes CB offers fast electron transfer kinetics, a feature particularly important in the case of electrode materials for sensing [8,9].

The accessibility of 3D printing technologies translates into exponentially growing popularity in electrochemical sciences where the technology allows for the easily accessible manufacturing of electrochemical energy storage devices [10–13], and sensing electrodes [14–19], and also electrochemical flow cells [20] or microscopy elements [21]. Rymansaib et al. [22], in an early work, have demonstrated an original procedure for formulation of a conductive filament composed of polystyrene (80%), carbon nanofibers (10%), and graphite microflakes (10%) for printing reusable electrodes suitable for differential pulse voltammetry detection of Pb^{2+} ions in aqueous media. Many

works have utilized commercially available filaments after that, and nowadays the application of purchasable, conductive carbon black-polylactide or graphene-polylactide 3D printed nanocomposite electrodes is flourishing.

The operation of electrochemical sensors is based on the measurement of the alteration of the electric current response resulting from redox processes at the electrode interface. The majority of reports on 3D CB-PLA electrodes show the necessity of their surface activation in order to be able to produce electrochemical response, however, nearly reversible charge transfer characteristics were also reported without activation in some studied cases [20,23,24]. The goal of the modification procedure is to etch the polymer matrix and reveal the conductive carbon filler. The most popular pre-treatment activation procedure for efficient electrode sensitisation so far is through immersion in dimethylformamide (DMF) [14,25,26]. There are a few recognised attempts to utilise different aprotic solvents, but so far, none of them provide comparable surface electroactivity [27,28]. As DMF and numerous other solvents are toxic or carcinogenic, there is an impetus to limit its use and to search for alternative activation routes. An alternative and possibly more environmentally friendly approach is through anodic and cathodic polarisation in neutral electrolytes, leading to small-sized sp^2-carbon domains increasing the electrode kinetics. Dos Santos et al. [29] used a graphene-enhanced, PLA-based filament from Black Magic 3D to manufacture disc-shaped electrodes, which were later electrochemically oxidized for 15 min by applying a potential of +1.8 V vs. SCE in phosphate buffer solution. A set of the electrodes was additionally electrochemically reduced after the oxidation, exhibiting high electroactive area and efficient electrochemical dopamine detection as a result. Browne et al. [30] have combined chemical activation in DMF (10 min) with electrochemical activation carried out in PBS (pH=7.2) at various potentials (1.5 V or 2.0 V or 2.5 V vs Ag/AgCl) over a range of times (0 – 250 s), with the optimum activity in hydrogen evolution reaction found at 2.5 V (150 s) of polarisation. The electrolysis of water at polarisation exceeding 6 V is a popular approach to remove the insulating thermoplastic via saponification [31,32] selectively, however some studies reveal that this treatment may cause excessive, irreversible oxidation of the electrode surface [24]. Another method for

functionalization of the electrodes is through metal electroplating [33]. Activation carried out under enzymatic activation using proteinase K [34] is also particularly promising.

Laser ablation is a popular method for removing portions of a material from solid surfaces. The laser treatment has not been widely used for the processing of PLA-conductive carbon composites, though several such attempts have been reported. Kanczler et al. [35] used a continuous wave fibre diode laser (wavelength of 970 nm, maximum power of 10 W) for a surface selective laser sintering of PLA powder mixed with microparticles of carbon black in order to manufacture biocompatible, porous 3D scaffolds promoting adhesion, proliferation, and differentiation of human bone cells. Paula et al. [36] deposited 10 μm thick films composed of polylactic acid and multilayer graphene fibres on glass substrates using a commercially available filament as a precursor. The resulting layers were illuminated with a $Ti:Al_2O_3$ femtosecond laser (central wavelength of 800 nm, pulses of 50 fs with a repetition rate of 5 MHz) to form electrodes having high-resolution patterns of interdigitated lines. The samples were characterised by an electrical resistivity of 5×10^3 Ωm and proved effective as electronic-tongue sensors, able to distinguish substances with different taste properties (H_2O, 1 mM NaCl, 1 mM sucrose, 1 mM HCl) without any superposition between them. Ongaro et al. [37] utilised a commercial Epilog Mini Helix CO_2 laser cutter (power, scanning speed, and frequency variable) to engrave microchannels on PLA sheets manufactured by compression molding. Inside the microchannels, electrode tracks were printed with an aqueous graphene ink. PLA monolayers were then bonded together with an adhesive tape to assemble a three-layer hybrid microfluidic device, which was characterised by cyclic voltammetry carried out at a 10 mV/s scan rate in the presence and absence of 5 mM potassium ferricyanide, and 5 mM potassium ferrocyanide. The resulting voltammograms displayed clear faradaic peak currents of the ferricyanide/ferrocyanide redox reaction.

The approach proposed by us has numerous advantages compared to typically exploited chemical or electrochemical surface activation protocols, such as localized surface modification, allowing the surface to be structured and patterns created. Locally enhanced surface activation may be helpful for

targeted CB-PLA electroplating. Moreover, laser ablation does not require hazardous chemicals or polarisation procedures and can even be introduced in some commercially available 3D printers.

The goal of this work is to discuss the capabilities of the laser ablation technique as an alternative route for the activation of 3D-printed CB-PLA electrodes. To do so, we present the influence of the laser operating parameters and the influence of the gas matrix during ablation on surface activation efficiency. To the best of our knowledge, this is the first attempt to use laser techniques for localised, selective PLA removal and electrode activation.

Finally, electrochemical caffeine assays based on 3D-printed CB-PLA electrodes were built and activated with the use of the optimized laser ablation procedure, and the detection limits compared to other carbon-based materials used for caffeine detection, including glassy carbon (GC), graphite, and boron-doped diamond (BDD) [38–40].

2. Materials and Methods

The material for 3D-printed electrodes used in this study was commercially available Proto-Pasta Conductive PLA. The given carbon filler content measured by thermogravimetric analysis was 26.4 wt.%, which resulted in 30 Ωcm electric resistivity (see *Supplementary Information* file, section S1). It should be noted that the structure of carbon black is analogous to that of graphene, also utilised in commercially available 3D printing filaments. The basic building unit of carbon black is graphene layers, arranged in parallel to the surface. Since the carbon black particles are spherical, the graphene layers are curved, introducing some heterogeneities in the electronic environment of the carbon atoms at the surface [41]. Moreover, the electrochemical properties of carbon black are on par with those manifested by thermally-reduced graphene oxide, exhibiting a valuable alternative in numerous electrochemical applications, due to carbon black's low cost and straightforward production process [42].

Flat electrodes were printed, with dimensions 10x10x2 mm, on an Ender 3 Pro 3D Printer (Ender, China). The 3D printing process parameters were as follows: printing temperature 200°C, bed temperature 50 °C, layer height 0.2 mm, nozzle diameter 0.4mm, printing speed 20 mm/s, infill density 100% and extrusion multiplier 1. Electrode designs were sketched in 123D Design (Autodesk, Inc., USA) and sliced with free Cura Ultimaker software (Ultimaker, Inc., USA). The electrodes were stored under atmospheric conditions. Electrochemical and physicochemical studies were carried out directly after the printing process. For the cross-section micrographs, a special series of samples with a 2x1 cm size and a notch at the bottom edge was printed. After laser processing, the plates were cooled in liquid nitrogen for about 60 seconds and then broken by applying bending force to the plates.

All chemicals were of analytical grade and used without purification. Caffeine, hexaammineruthenium(II) chloride ($[Ru(NH_3)_6]^{2+}$), phosphate-buffered saline (PBS), and potassium chloride KCl were purchased from Sigma-Aldrich. All solutions were made from deionised water. The PBS was adjusted to a pH of 7.0 using hydrochloric acid.

The ablation of the 3D-printed CB-PLA electrodes was carried out using a pulsed LaserBlast 500 Nd:YAG laser (Quantel, France) operating at 1064 nm and a 6 ns pulse duration. The laser was equipped with diffractive optics delivering a Top Hat beam profile and square laser spot. Surfaces of the samples were scanned with a laser spot of 5×5 mm. Three different values of energy density (*ED*) – 0.64, 0.9 or 1.15 Jcm^{-2} – were tested. To minimise thermal effects, the laser pulse repetition was set to 2 Hz. Moreover, the electrodes were treated with a diverse number of pulses (*n*) – 10, 20, or 30. The atmosphere of the laser ablation was also under examination, with activation carried out in an ambient atmosphere, or an inert gas (helium, purity 5.0). The use of He instead of Ar as a shielding gas was dictated by the much higher thermal conductivity of He (156.7 mW mK^{-1}) compared to Ar (17 mW/mK^{-1}) to minimize the thermal effects caused by the ns laser pulses. The variability of *ED*, *n*, and the atmosphere yielded 18 combinations of the parameters and enabled a thorough study of their impact on the structure and performance of the examined 3D-printed electrodes.

Scanning electron microscopy with a variable pressure chamber (VP-SEM) was selected to observe the topography of the surfaces of the samples and to assess how deep the laser penetrated into the electrodes during the ablation. These studies were performed with a S-3400N microscope (Hitachi, Japan), using a 25 kV accelerating voltage and under a pressure of 90 Pa. Before the examination, the electrodes were coated with nanometric layers of gold to increase their conductivity.

The chemical composition of selected electrodes was examined with X-ray photoelectron spectroscopy (XPS) and Raman spectroscopy. The XPS analyses were carried out using an Escalab 250Xi multispectroscope (Thermo Fischer Scientific, USA). The spectroscope was equipped with a monochromatic AlKα source. The high-resolution spectra in the *C1s* and *O1s* binding energy range were collected with a pass energy of 15 eV and using an X-ray spot diameter of 250 μm. Charge compensation was controlled through a low-energy electron and Ar^+ ion flow by a flood gun. The Raman analysis was performed using a Raman microscope (InVia, UK). Spectra were recorded in the range of 120–3200 cm^{-1} using an argon-ion laser emitting at 514 nm and operating at 1% of its total power (50 mW) to avoid PLA melting. Data were smoothed (with a Savitzky-Golay filter, 15 points, 2nd polynomial order). Each sample was analysed at five randomly selected points on its surface. The spectrum of each point on the sample was recorded as an accumulation of five scans. The exposition time of a single scan was set to 20 s. For the Raman analysis of a sample cross-section, the CB-PLA electrodes were cooled down in liquid nitrogen and mechanically broken. On the sample cross-section, Raman spectra were recorded in the middle of the sample thickness and near the surface irradiated with a laser, using a 100x objective lens microscope. The contact angle measurements were conducted using Drop Shape Analyser (DSA) 100, (Krüss, Germany). All analyses were performed at room temperature, using 2 μm deionised water drop volume. The contact angles were determined using the sessile drop method. The analysis of the shape of the drop was performed using the Young-Laplace fitting method. All measurements were repeated ten times.

Every activated electrode was subjected to electrochemical analysis to verify the kinetics of the charge-transfer process due to activation. Electrochemical impedance spectroscopy (EIS) and cyclic

voltammetry (CV), and differential pulse voltammetry (DPV) studies were performed on an Autolab 302N potentiostat (Metrohm, Switzerland), controlled by the NOVA 2.4 software. The electrochemical studies were carried out in a three-electrode setup, with CB-PLA as the working electrode, Ag|AgCl (3 M KCl) as the reference electrode, and a Pt wire as the counter electrode after initial conditioning for 10 minutes. Studies were performed in 5 mL electrochemical cells in naturally aerated electrolytes. The EIS activation efficiency tests were performed in 0.1 M KCl, and in the 10 kHz – 0.1 Hz frequency range, with 15 perturbation signals per frequency decade. The amplitude of the perturbation signal was 10 mV and the measurements were carried out in potentiostatic mode, under open circuit potential conditions. The detection of caffeine was performed in 0.01 M PBS solution (pH = 7.0) in increasing concentrations of caffeine from 0.01 mM to 1 mM. The CV and DPV procedures for caffeine detection were carried out in the polarisation range from +0.5 to +1.6 V vs Ag|AgCl (3M KCl). All the CV scans within the manuscript were conducted at a 100 mVs^{-1} polarisation scan rate.

3. Results and discussion

3.1. Influence of laser energy density, number of pulses, and ablation gas atmosphere

The efficient 3D-printed CB-PLA composite electrode activation process is based on the effective removal of the surface polymer matrix, which uncovers the conductive carbon filler, developing electrochemically active surface area (EASA) of the electrode, while avoiding oxidation processes and degradation of the polymer matrix which lead to sub-optimal electrode characteristics. The process can be optimised through careful consideration of the internal factors affecting laser ablation, to be carried out as the first step of this study. Different laser energy densities (*ED*) and the number of short irradiation cycles (*n*) were tested. The effect of the proposed activation conditions was verified using EIS analysis, comparing the results with the CB-PLA electrode before the activation.

The Bode plots in **Fig. 1** show the impedance modulus |Z| vs. applied perturbation frequency for each studied CB-PLA electrode, with the corresponding phase angle variation (*θ*) shown in the inset. When

comparing different laser energy densities, the smallest impedance modulus was observed at $ED =$ 0.64 Jcm^{-2} and rises with the energy density increase. This is best noticed at the lowest frequency range, where contribution from the electric double layer charging dominates the $|Z|$ value. Regardless of the applied laser operating parameters, the activation process lead to a decrease in the electrode resistance by not less than two orders of magnitude, down from approx. 4.20 MΩ, recorded for the inactive CB-PLA electrode. The impedance modulus recorded at $f = 0.1$ Hz after laser ablation treatment was equal to 2.27, 4.32, and 8.90 kΩcm^2, for 0.64, 0.90, and 1.15 Jcm^{-2} laser energy densities, respectively. The analysis of the phase angle spectrum reported in the inset of **Fig. 1a** shows that the impedance spectra of each surface-modified CB-PLA electrode was characterised with a quite similar value of the time-constant, evidenced by a small shift towards the lower frequencies range when comparing between the most efficient activation at 0.64 Jcm^{-2} and different laser energy densities. This outcome suggests a similar surface activation mechanism for each of the activated CB-PLA electrodes.
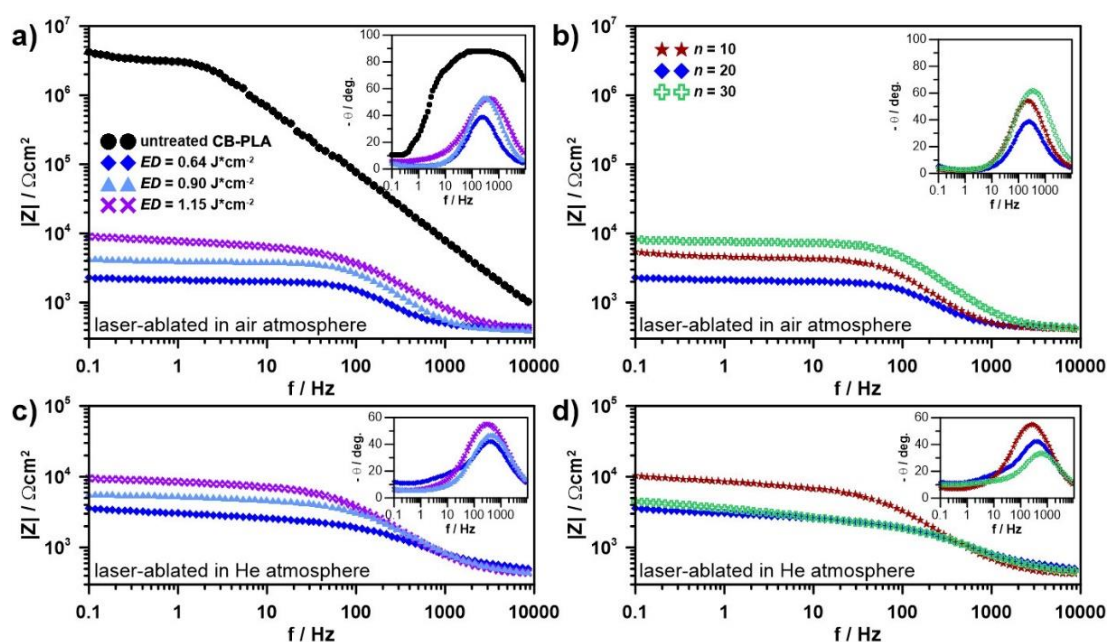

Figure 1. Impedance Bode plots (phase shift plots in the inset) registered before and after laser-induced activation of CB-PLA electrodes a,b) in air, c,d) in He atmosphere; studies carried out after ablation with various a,c) laser energy densities ED ($n = 20$), b,d) numbers of short laser pulses n ($ED = 0.64$ Jcm^{-2}). Studies were carried out in 0.1 M KCl, after 10 minutes of electrode conditioning.

The number of laser pulses appears to have some effect on the CB-PLA EASA, while the most prolonged ablation duration results in the highest recorded impedance modulus (and the electrode resistance), equal to 7.99 kΩcm^2. On the other hand, a too short irradiation cycle results in partial surface area activation.

In order to evaluate the influence of the PLA oxidation on the laser-activated CB-PLA electrode we performed the same procedure in a noble gas matrix (helium). Interestingly, the inert gas atmosphere had a negligible influence on the electrochemical activity after laser ablation treatment, thus suggesting that surface oxidation was not the cause of the hindered electroactivity at higher energy densities (see **Fig. 1c**).

One crucial difference emerged comparing the cross-section topography of the CB-PLA electrodes treated with various laser energy densities, which is the roughness of the laser-etched crater edges, seen in the insets of **Figs. 2c and 2d**. The kinetic energy of the molecules in the plasma translated into temperature-induced vibrations and rotations within the ablated PLA, whose nature was more local at low energy densities. At low energy densities, the ablation was characterised by the more local character of material degradation and ragging the edges of the laser-etched craters. The higher the energy density, the larger the areas of elevated temperature under laser interaction. When a laser with a certain energy irradiated the CB-PLA surface, the surface became molten, breaking the polymer chains under the action of the re-melting mechanism, and making the surface material flow into unfilled spots. A similar mechanism was described in detail in studies dedicated to PLA laser polishing [43,44]. Based on the above-presented mechanism and SEM cross-sections, we hypothesise that re-covering of the active carbon filler taking place at higher laser energy densities is restraining the electrochemically active surface area. The hypothesis is in good agreement with similar EIS findings obtained in air and He atmospheres.
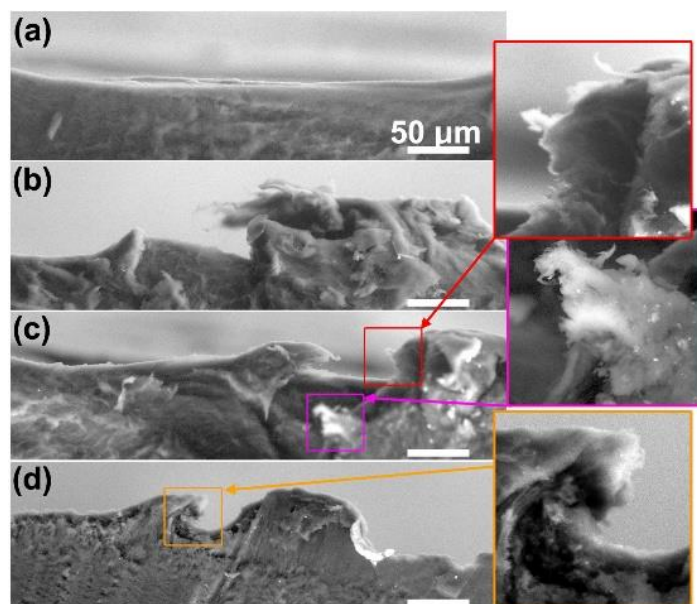
Figure 2. Cross-section of CB-PLA electrodes: a) untreated for reference, b–d) subjected to laser ablation in air atmosphere (n = 20) at various energy densities *ED*: b) 0.64 Jcm^{-2}, c) 0.90 Jcm^{-2}, d) 1.15 Jcm^{-2}.

The VP-SEM micrographs presented in **Fig. 2** also reveal that 20 short laser pulses are enough to penetrate the CB-PLA material approximately 70–100 µm underneath the surface, and that the penetration depth does not depend greatly on the laser energy density. The above result allows us to conclude that the CB-PLA electrode roughness is similar in each studied case and does not have a key influence when it comes to the development of the electrochemically active surface area (EASA).

On the other hand, carrying out the ablation process in a He atmosphere had a visible effect on the CB-PLA electroactivity when considering the influence of the number of laser pulses. Here, unlike in the case of air-assisted irradiation, the detrimental effect of the prolonged laser ablation was significantly lower, as testified by the impedance results in **Fig. 1d**. These findings suggest hindering the Faradaic conductivity by carbon species with ablation time and in the presence of oxygen, as will be further discussed based on Raman spectroscopy analyses. The electrode surface's excessive oxidation is hypothetically the cause of more irreversible charge transfer observed after anodic electrochemical activation of 3D printed CB-PLA electrodes [32].

The micrographs in **Fig. 3** allow us to compare the activated CB-PLA electrode topography and depth of penetration depending on the gas atmosphere of the ablation process. The comparison was performed under optimised activation process operating conditions ($ED = 0.64$ Jcm^{-2}, $n = 20$). When studying the topography at low magnifications (x100, **Fig. 3a**) one can spot the remnants of the partially etched polymer matrix, seen as the bright colours due to its non-conductive nature. The gas atmosphere used for the activation process did not seem to have a significant influence on the topography of the CB-PLA electrode. **Figs 3b** and **3c** present the micrographs in cross-section, revealing a similar penetration depth, in both cases reaching 30–40 µm. Furthermore, the high magnification micrographs of the activated CB-PLA surface show highly similar effects of the polymer matrix removal (**Figs 3d,e**). Here, the light-green colour highlights the carbon black agglomerates, uncovered by the laser ablation treatment [45]. It was evenly distributed at the composite surface. Its local amounts at certain electrode areas may vary, regardless of the studied environment.
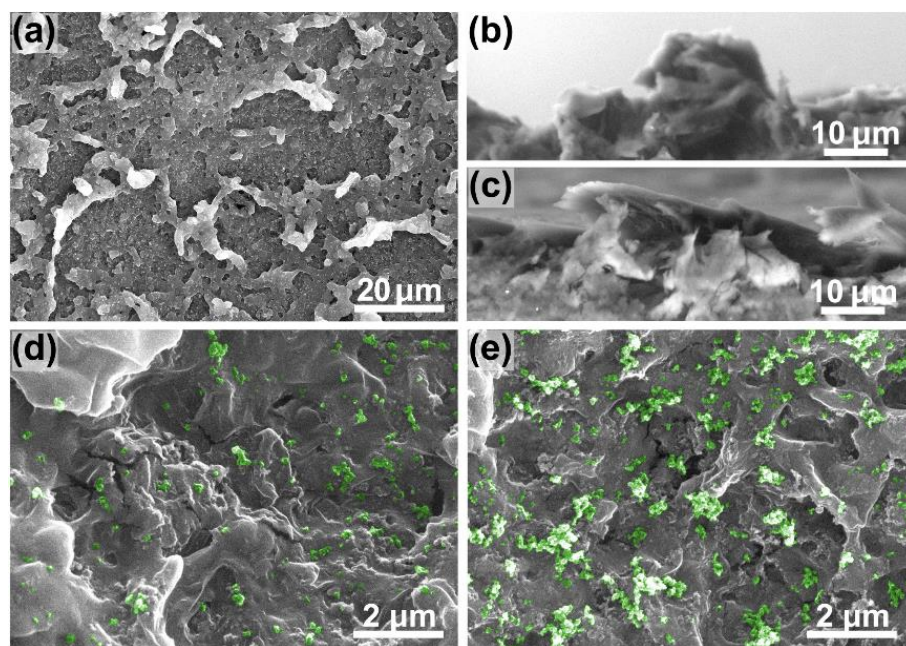
Figure 3. Micrographs showing a,d,e) topography; and b,c) cross-section of CB-PLA samples ablated in different atmospheres: a,b,d) air atmosphere; and c,e) He. Ablation parameters: $n = 20$, $ED = 0.64$ Jcm^{-2}.

The reference Raman spectra were recorded at the cross-section of the laser-irradiated electrode (parameters of ablation: $n = 20$, $ED = 1.15$ Jcm^{-2}), in an area completely unaffected by the laser. This

region of the electrode was considered a core of the sample, an area composed of CB-PLA which was melted during the printing process, but immediately thereafter covered with successive layers of the material, greatly limiting its exposure to the ambient air during the cooling. Next, the Raman spectra were recorded for a surface of the untreated electrode, as well as for electrodes processed with a laser using an energy density of 1.15 Jcm^{-2} and a dose of 20 laser pulses per electrode surface (1 cm^2), in air and helium atmospheres. The Raman spectra are dominated with D and G bands centered at 1361 and 1596 cm^{-1}, respectively, and derived from carbon black filling [45,46], as seen in **Fig. 4a**. The D band is associated with disordered sp^3-hybridised carbon featured as defects or impurities in the carbon materials, the G band is associated with the E_{2g} phonon modes of the sp^2-bonded carbon, and a broad 2D peak around 2722 cm^{-1} is the second order of zone-boundary phonons [41,47,48]. A (D + G) band at 2957 cm^{-1} was due to the defects in the sp^2 sites. The I2D/IG ratio changed for samples processed with the laser. For pristine material, the value of the I2D/IG ratio was about 0.12 and increased to 0.14 and 0.20 for samples processed with laser in air and helium atmospheres, respectively.

The most visible effect of thermal processing of CB-PLA was the increase of background photoluminescence. In the core of the sample, the PLA material was homogeneous, which was confirmed by a negligible value of the standard deviation. Additionally, no differences were observed between the spectra recorded in the middle of the sample's cross-section and the proximity of the surface. It should be noted that the surface of the sample, even if unprocessed by the laser, showed increased background fluorescence in comparison to the polymer analysed in the core. This effect can be explained by PLA oxidation processes occurring on the surface as a result of contact of the molten material with air. The level of the background photoluminescence increased further after laser processing in the air. This phenomenon, which originates from structural defects caused by thermal quenching and re-solidification [49,50], indicates degradation of the PLA during laser ablation in the presence of oxygen. The opposite effect was observed in the case of laser ablation in the helium atmosphere where the background photoluminescence decreased in comparison to the level recorded for the untreated surface. This can be explained by laser removal of the top layer of the material. At

the same time, degradation processes during ablation in the oxygen-free atmosphere occurred less intensively.
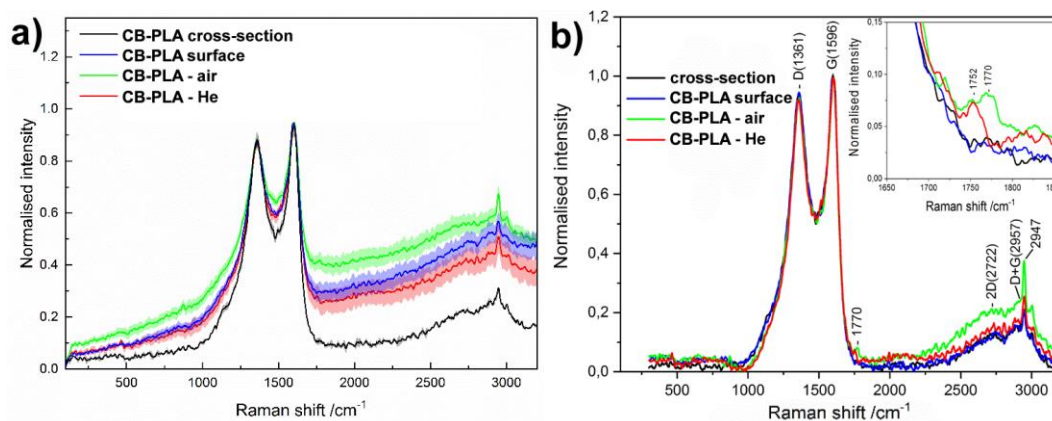
Figure 4. a) Raman spectra recorded for: printed CB-PLA electrode cross-section, unprocessed surface of 3D printed electrode, and electrode surface after laser treatment in air and helium atmosphere. Pattern indicates the standard deviation of spectra measured in different points; b) Raman spectra after removing background photoluminescence, with the zoomed-in 1650 to 1850 cm^{-1} spectral range in the inset.

Removing the background photoluminescence, as seen in **Fig. 4b**, exposes the weak Raman bands of the polymer. The Raman spectra of the laser-processed CB-PLA expose weak bands in the region from 1750 to 1776 cm^{-1} (**Fig. 4b** – inset). According to the literature, bands at 1750, 1766, 1770, and 1776 cm^{-1} can be assigned to C=O stretch vibrations. Additionally, the band located at 1770 cm^{-1} is characteristic of the amorphous phase of PLA polymer and its intensity can be used to determine the crystallinity of the material [51]. In our experiment, an evident increase of 1770 cm^{-1} band is observed for samples laser irradiated in the ambient air atmosphere. For the samples irradiated in the He atmosphere, the Raman signal at 1770 cm^{-1} is much weaker. In general, the appearance of the amorphous phase after laser irradiation can be explained by a high cooling rate due to the large temperature gradient induced by laser ablation. It can be supposed that the increased intensity of the band at 1770 cm^{-1} in the case of samples irradiated in the presence of oxygen in the ambient air may be associated with an increased number of defects in the PLA structure caused by oxidation processes. In the spectral range of 2800–3000 cm^{-1}, CH$_3$ symmetric (2881, 2947 cm^{-1}) and asymmetric (3000 cm^{-}

[1]) bands can be observed. The increased intensity of the band centered at 2947 cm^{-1} correlates with the decrease of PLA crystallinity [51].

Next, X-ray photoelectron spectroscopy was used to evaluate the surface chemistry modification as a result of CB-PLA irradiation in air and helium atmospheres. These studies were compared with the surface chemistry of the reference freshly 3D-printed CB-PLA electrode and are collectively presented in **Fig. 5**.

The high-resolution XPS analysis in the C1s energy range revealed a complex multicomponent spectrum, with not less than four different spectral components, partially overlapping each other (**Fig. 5a**). Taking into consideration PLA's chemistry, three different carbon chemical states are to be expected, namely C-C, C-O, and C=O, with an expected ratio of 1:1:1. These three chemical states are represented by *C2*, *C3*, and *C4* peaks, respectively. It can be noticed that in contrast to the theoretical 1:1:1 ratio expected for pure untreated PLA, the *C2* C-C/C-H peak is significantly higher, indicating an excess of hydrocarbons on the untreated PLA surface, to be explained by the contribution of adsorbed adventitious hydrocarbons contamination from the atmosphere [52,53]. The primary component from sp^2-carbon within the conductive carbon black filler (so-called graphite peak) is expected to appear negatively shifted versus the aliphatic hydrocarbons component [41,45,54,55]. Indeed, the *C1* peak, reflecting the share of surface carbon black filler, is shifted at -1.1 eV vs the *C2* peak. Its share in the reference sample is on par with the *C2* component, demonstrating its significant amount in the most outer part of the electrode surface (XPS depth analysis was approx. 5 nm).
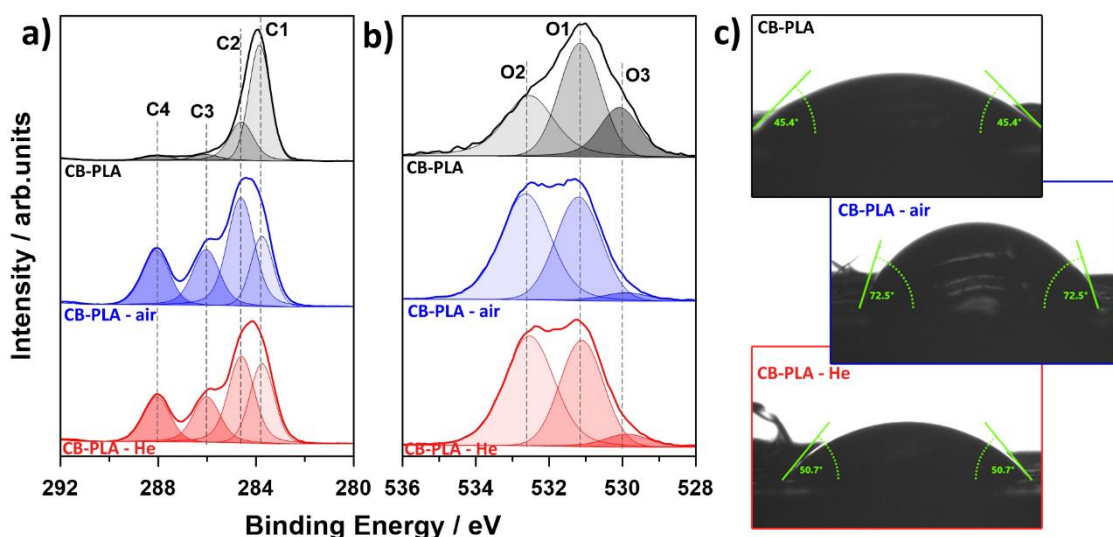
Figure 5. Surface carbon and oxygen chemistry of 3D-printed reference CB-PLA before modifications, and CB-PLA electrodes after laser ablation in air and He atmospheres; a) C1s and b) O1s high-resolution XPS spectra. c) contact angles measured for the corresponding CB-PLA electrodes.

The O1s spectra recorded for the reference CB-PLA electrode were also deconvoluted using four spectral components (**Fig. 5b**). The two dominant ones – *O1* and *O2* – located at binding energies of 531.2 and 532.6 eV, should be ascribed to C=O and C-O bonds, respectively [53,56]. The *O1*:*O2* ratio is 0.8:1, which is lower than the theoretical 1:1 ratio expected of PLA. Again, the higher share of C=O bonds is to be explained with adventitious carbon contamination. The *O3* is problematic in unequivocal identification and may hypothetically represent some metal-oxygen bonds in the impurities introduced by the CB-PLA filament manufacturer [57]. Finally, the last component is only present in the spectra recorded for the reference CB-PLA, and is most likely connected with surface-chemisorbed water molecules resulting from prolonged air exposure of the 3D printed electrodes [56,58]. The details of the XPS analysis are summarised in **Table 1.**

When comparing the CB-PLA electrode pre-treated by laser ablation in the air or a helium atmosphere with the reference CB-PLA, one can see a few key differences in the contribution of the individual components. Interestingly, the contribution of carbon black nanoparticles, represented by the *C1* peak, decreases for ablation in the air atmosphere, which is assisted by the growth of the contribution of the *C2* peak. The *C2*:*C3*:*C4* ratio changes from 1.5:1.1:1.0 for the reference sample up to 2.2:1.1:1.0,

which suggests the increasing share of hydrocarbon contaminants. Simultaneously, the amount of the PLA signal at the electrode surface slightly decreases, which can be directly tracked through the contribution pf the C-O and C=O C1s peaks. Ablation in the air is assisted by higher surface oxygen concentration, adsorbed, or chemically bonded, as can be seen in **Table 1**.

Table 1. Surface chemical composition (in at. %) of the 3D printed CB-PLA electrode, as well as after laser ablation in air or helium atmosphere, based on the high-resolution XPS analysis.

Chemical state		BE / eV	Reference	Laser ablated	
				in air	in helium
C1s	*C1*	283.7	22.8	16.9	27.5
	C2	284.8	22.2	28.2	23.9
	C3	286.0	15.9	13.8	11.9
	C4	288.1	14.5	12.7	11.5
O1s	*O1*	531.2	9.1	12.3	11.7
	O2	532.6	11.8	14.4	11.6
	O3	529.9	1.0	1.8	1.9
	O4	534.1	2.6	--	--

However, a different explanation for the significantly higher contribution of the *C2* peak is more plausible and supported by both the literature and the Raman spectroscopy data. The filler may be partially oxidised as a result of the laser treatment, with a consequence in a shift of the C1s peak towards higher binding energies [41,59]. Assuming the correctness of the hypothesis, the formation of oxidised carbon black would explain a significantly decreased amount of the *C1*:*C2* ratio (from 1.0:1.0 for the reference sample, down to 1.0:1.7 for the CB-PLA sample after ablation in the air atmosphere).

CB is typically inactive toward oxygen reduction reaction [60]. Oxidized CB displays electron-accepting surface regions as revealed by Harbour et al. [61]. Nevertheless, the electrochemical reduction of these sites was manifested by an electron transfer to the carbon clusters. Oxidation of carbon black yields an enhanced electron transfer rate constant [62] being also responsible for improving the electrochemical performance. It was found that oxidation resistivity of carbon black is

lower than other carbon materials (e.g., CNT [63]) applying thermal or wet treatment. Thanks to the laser treatment nature, it could efficiently induce groups with oxygen content at CB surface.

Further evidence is provided when analysing the surface chemistry of the CB-PLA after irradiation in the helium atmosphere. First and foremost, the share of the *C1* spectral component is the most prominent for this sample, among all of the studied CB-PLA electrodes (27.5% vs 22.8 for the reference CB-PLA and 16.9 for the CB-PLA ablated in the air atmosphere). At the same time, different studies on pure PLA reveal the C1s peak ratio to be significantly closer to the theoretical 1:1:1 PLA if laser-treated in a He atmosphere [53]. Notably, the surface PLA removal and activation seem to be even more efficient in our case, as testified by a further decrease of the *C3* and *C4* components. Finally, the contribution of the *C2* peak is similar to the reference sample.

The measurement of the contact angle is a very useful tool, providing information about changes in the polarity of the target surfaces, before as well as after their modification [64,65], and therefore, we decided to carry out contact angle studies of the CB-PLA electrodes. The results of this analysis reveal the dependence of the wettability on the preparation method (**Fig. 5c**). In all cases, the value of the obtained contact angle did not exceed 90°, indicating that all investigated CB-PLA surfaces are hydrophilic [66]. The contact angle determined for the reference CB-PLA electrode before laser ablation treatment was 45.4°, which is slightly lower than the values reported in the literature due to PLA remelting during the 3D printing operation [67–69]. Next, after laser ablation in the air atmosphere, the value of the contact angle increased to 72.5°, which directly indicates that the ablation in the air atmosphere caused a decrease in surface hydrophilicity. On the other hand, changes in hydrophilicity occurring at the CB-PLA surface after ablation in the He atmosphere were not so significant in comparison to the reference CB-PLA, and the contact angle reached 50.7°. The contact angle studies follow the XPS results, testifying to minor CB-PLA surface chemistry modification as a result of laser ablation in both the air and He-based atmospheres.

Lu et al. [70] reported that carbon black exhibits a water contact angle of 89°, while oxidised carbon black displays hydrophilic contact angles of approx. 60° [71], due to the incorporation of carbonyl and

carboxyl polar groups. Furthermore, the contact angle of PLA/CB composites was reported to achieve *ca.* 45° thanks to decay and dissipation of static electricity of pristine PLA having a contact angle of approx. 83° [72].

We observed that air-based laser ablation results in a stronger hydrophobic surface than treatment in the noble gas. This fact suggests that more pristine carbon black is exposed by air-based treatment, while this finding is not fully supported by XPS. Wetting interactions reveal a complex nature here thanks to the hybrid composite structure inducing heterogeneous distribution of surface free energy. This led us to the conclusion that contact angle studies of the ablation process could be applied only for qualitative studies supporting data extracted by XPS or Raman due to the developed surface morphology along with the complex structural composition.

Finally, the electrochemical characterization of the fabricated, laser-ablated CB-PLA electrodes was made to benchmark our surface activation protocol against the available literature studies (listed in *Supplementary Information* file, section S2 and S3). $[Ru(NH_3)_6]^{2+/3+}$, possessing the outer-sphere electron transfer mechanism, was utilized as the redox-active probe.
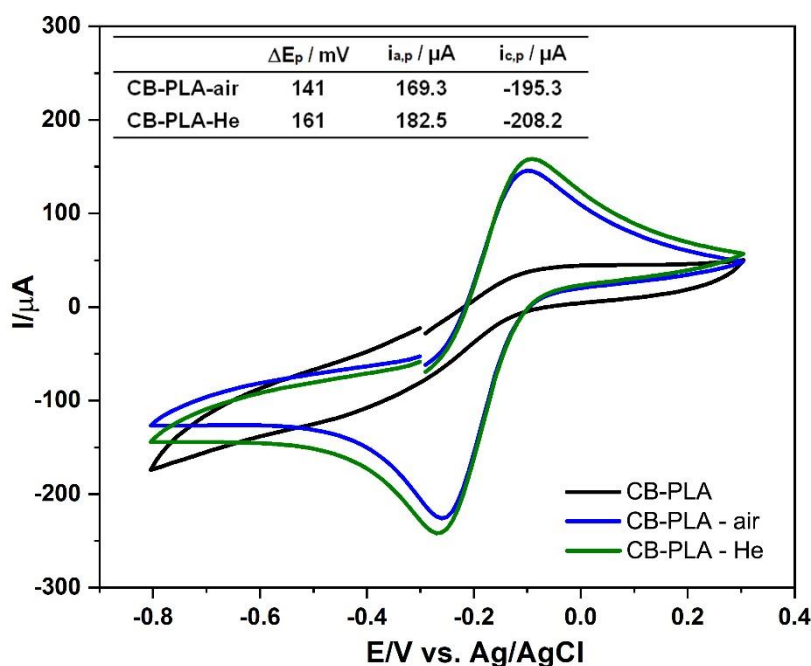
Figure 6. Cyclic voltammetry measurements of CB-PLA electrode before and after activation in air or helium atmosphere. Scan rate 100 mV/s. Electrolyte 0.1 M KCl + 1 mM $[Ru(NH_3)_6]^{2+}$. Laser ablation parameters: $n = 20$, $ED = 0.64$ Jcm^{-2}.

It could be observed that the electrochemical response of the redox probe is nearly non-existent before the surface activation. The electrochemical activity of the CB-PLA electrode after ablation in He can be explained by effective PLA polymer layer removal by the laser beam, thus developing EASA to the highest extent. The laser ablation allows for an efficient surface electrochemical activation, testified by the well-developed $[Ru(NH_3)_6]^{2+/3+}$ oxidation/reduction peaks. The values of the peak separation ΔE_p suggests that the charge transfer process is close to reversible with the anodic-to-cathodic peak current ratio $i_{a,p}/i_{c,p}$ close to 1 (0.87 and 0.88 for air and He atmosphere, respectively).

Next, the Nicholson method was applied to determine the heterogeneous rate constant (k^0_{obs}) between the 3D-printed CB-PLA and $[Ru(NH_3)_6]^{2+/3+}$ probe, based on eq. (1) [29]:

$$k^0_{obs} = \left[2.18\left(\frac{D\alpha n F v}{RT}\right)^{1/2}\right] exp\left[-\left(\frac{\alpha^2 n F}{RT}\right)\right]\Delta E_p \tag{1}$$

where D is the diffusion coefficient ($9.1*10^{-6}$ cm^2 s^{-1}), n is the number of electrons transferred, α is the charge transfer coefficient (assumed to be 0.5), v is the applied scan rate, ΔE_p is the peak-to-peak separation, R is the gas constant, F is the Faradaic constant and T is the temperature.

The heterogeneous rate constant k^0_{obs} of CB-PLA electrodes is assumed to be $2.42*10^{-3}$ and $2.76*10^{-3}$ cm s^{-1} for the surface activation carried out in air and He atmospheres, respectively. A very similar electron transfer kinetics regardless of the gas atmosphere suggests comparable exposure of the carbon black species as a result of the treatment. Moreover, the obtained k^0_{obs} value is comparable and often higher than in the previous reports (see *Supplementary Information* file, section S3), which confirms the competitive efficiency of laser ablation treatment compared to other surface activation methods.

3.2. Evaluation of laser-activated CB-PLA electrode for caffeine detection

The caffeine electrochemical process is presented in **Fig 7b**. This mechanism includes four electrons and four protons and consists of two steps. The first step is slow and leads to the formation of the substituted derivative of uric acid, while the second step is fast and causes further oxidation and formation of uric acid 4,5-diol analog that undergoes further fragmentation as a consequence of oxidation [73,74] (see *Supplementary Information* file, section S4). Thus, the detection of caffeine present in an analyte solution can be easily performed by measuring its electrochemical response. Two electrochemical techniques were used for this task, namely CV and DPV, and the obtained results are presented in **Figs 7c** and **7d**, respectively. This test was performed in 0.01 M of PBS solution (pH = 7.0) containing 1 mM of caffeine. The peak potentials of caffeine oxidation appear at 1.5 V and 1.4 V vs Ag|AgCl for CV and DPV respectively, corroborating other findings [75–78].

The caffeine oxidation peaks are best developed at the CB-PLA electrode, when activated in a He atmosphere, and reach over 200 µA, in comparison to the remaining studied samples (at 100 mVs^{-1} scan rate). The electric current in caffeine oxidation peak is incomparably smaller for the CB-PLA after ablation in the air atmosphere, as the reference untreated CB-PLA electrode remained electrochemically inactive. A similar conclusion can be drawn from the DPV experiment.

There is a significant difference in the faradaic currents registered during caffeine oxidation when compared to $[Ru(NH_3)_6]^{2+/3+}$ between CB-PLA electrodes activated in air or He atmosphere. Caffeine oxidation is a multi-step process, which follows a complex inner sphere electron transfer mechanism dependent mainly on the level of oxidized surface functional groups, different for both studied electrodes, as revealed by XPS and Raman analyses.

One should take into consideration that factors such as electrode contamination with caffeine oxidation products, or operating near the polarisation range reported for the electrochemical CB-PLA activation [79,80] may have some influence on the oxidation kinetics during the consecutive polarisation cycles.
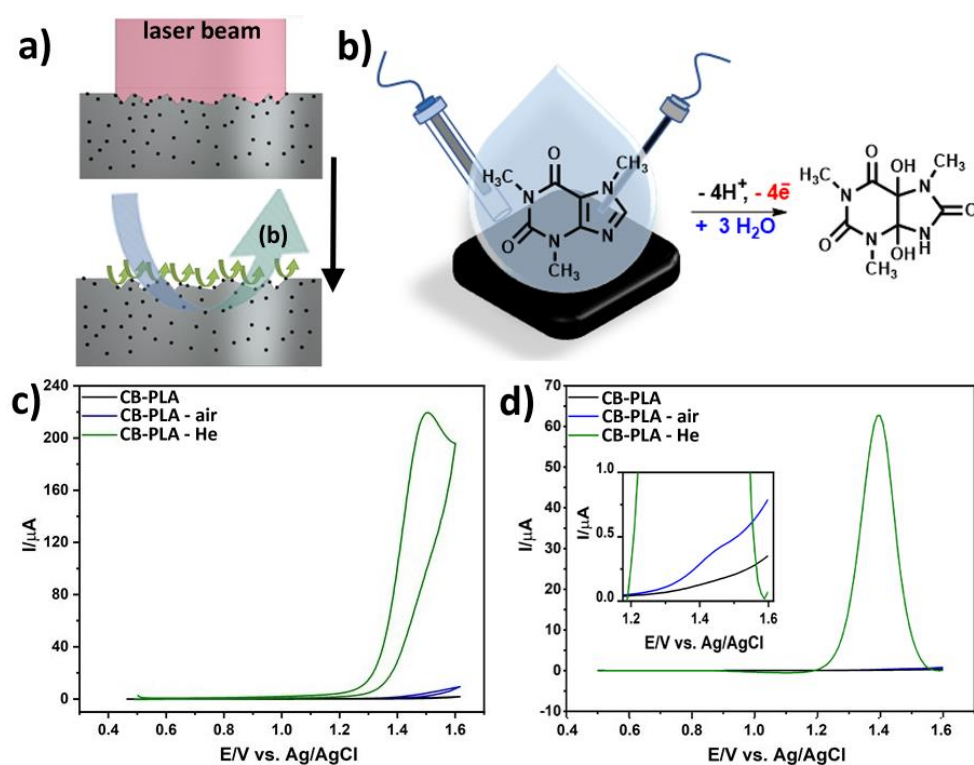
Figure 7. a,b) Mechanism of electrochemical caffeine oxidation at the CB-PLA electrode, c) CV and d) DPV scans for caffeine detection at different CB-PLA electrodes. Measurements for 1 mM caffeine concentration in 0.01 M PBS, before and after CB-PLA electrode activation in air or helium atmosphere. Laser ablation parameters: $n = 20$, *ED* $= 0.64$ Jcm^{-2}.

The above-presented experiment allowed us to verify the highest utility of the CB-PLA surface activated in the He atmosphere. The determination of caffeine was performed in the caffeine concentration ($C_{caffeine}$) range from 0.01 mM to 1 mM. The CV measurements of caffeine oxidation indicate that the peak current ($I_{caffeine}$) in the obtained voltammograms increases linearly with the increasing caffeine concentration (**Fig. 8a**). The relationship between the caffeine oxidation current and the caffeine concentration is presented in the inset (**Fig. 8a** inset). The CB-PLA electrode after ablation in He expresses a good linear response with the linear regression given by eq. (2):

$$I_{caffeine} \ (\mu A) = 0.2110 \ [C_{caffeine} \ (M)] + 6.727 \tag{2}$$

and with the correlation coefficient ($R^2 = 0.990$). The limit of detection (LOD) was calculated to be 0.49 µM (with the S/N ratio of 3). The obtained detection limit is comparable with the LOD obtained

for modified glassy-carbon electrodes by CV [81] or square-wave voltammetry [82], which were found

to be very satisfactory.
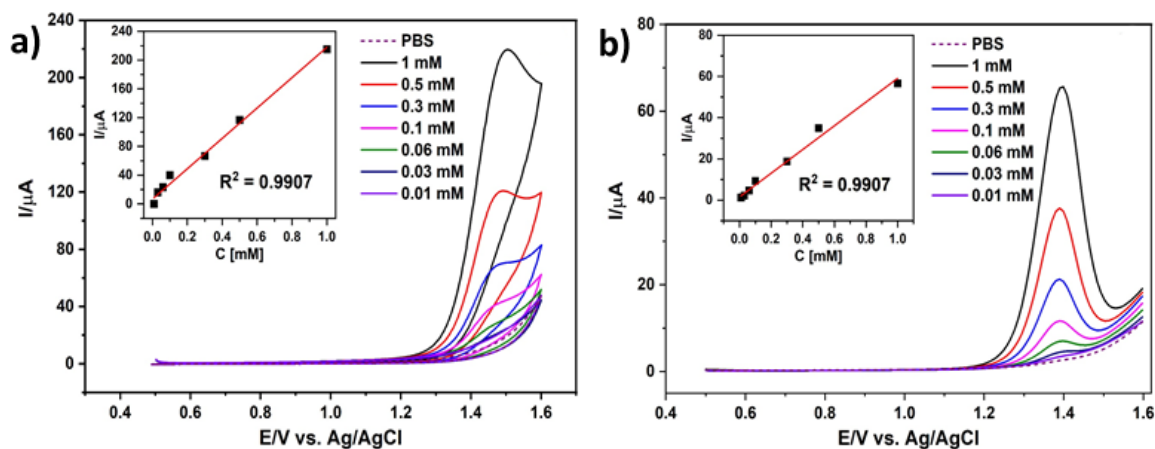
Figure 8. CV a) and DPV b) scans for caffeine detection at the CB-PLA electrode activated in helium atmosphere. Laser ablation parameters: $n = 20$, $ED = 0.64$ Jcm^{-2}. Electrolyte 0.01 M PBS.

The DPV experiment provides similar result as the CV studies; the caffeine determination by DPV is

shown in **Fig. 8b**. The relationship between the caffeine oxidation current and the caffeine

concentration is presented in **Fig. 8b** inset. A linear response was also observed in this case, with the

regression equation given by eq. (3):

$$I_{caffeine} \text{ (µA)} = 0.0636 \, [C_{caffeine} \text{ (M)}] + 2.288 \tag{3}$$

and with correlation coefficient ($R^2 > 0.99$). The LOD was calculated to be 0.40 µM (S/N = 3), which

is very good compared to other studies using DPV [38,83,84]. The obtained CV and DPV results

confirm the high efficiency and good reproducibility of quantitative evaluation of the presence of

caffeine with the use of CB-PLA electrodes after surface activation by laser ablation in a He

atmosphere.

4. Conclusions

In summary, investigations focused on the laser treatment of Proto-Pasta Conductive PLA electrodes

revealed the high efficiency of the ablation process enabling electro-activation of their surfaces. The

laser-induced activation process involves the effective removal of polymer matrix from the 3D printed CB-PLA composite electrode surface suppressing carbon black oxidation and degradation of the polymer matrix. Microimaging exhibited that just 20 short laser pulses were enough to achieve the abovementioned effect, penetrating the electrode to a depth of approx. 100 μm.

It was found that the penetration depth does not depend on the laser energy density, but much more on the treatment repetition and process atmosphere. The physical effect of CB-PLA surface melting and breaking the polymer chains during re-melting processes induced by laser irradiation played the main role during the surface treatment.

The laser ablation procedure was conducted in an inert gas matrix (helium) to avoid the CB-PLA oxidation process in the air, which hinders the charge transfer through the electrode/electrolyte interface. Both the achieved contact angles and XPS data showed the minor influence of the laser treatment in a noble gas atmosphere on the modification of the CB-PLA chemistry, while delivering large electrochemically active surface area. The formation of oxidized carbon black phases at the CB-PLA electrode was achieved during the air-assisted ablation process similar to the thermal treatment approach resulting in hydrophilic contact angles. The estimated heterogeneous rate constant of $2.42*10^{-3}$ and $2.76*10^{-3}$ cm s^{-1}, obtained for $[Ru(NH_3)_6]^{2+/3+}$, after CB-PLA laser ablation in air and He atmosphere, respectively, was found to be competitive versus other surface activation protocols.

The electroanalytical performance of laser-treated CB-PLA electrodes was proven through the caffeine detection process involving the CV and DPV techniques. The caffeine oxidation peaks were considerably enhanced at the CB-PLA electrode activated in the helium atmosphere in contradiction to the air-assisted laser activation or freshly printed untreated surfaces.

References

[1] K. Formela, L. Zedler, A. Hejna, A. Tercjak, Reactive extrusion of bio-based polymer blends and composites – Current trends and future developments, Express Polym. Lett. 12 (2018) 24–57. https://doi.org/10.3144/expresspolymlett.2018.4.

[2] T.D. Ngo, A. Kashani, G. Imbalzano, K.T.Q. Nguyen, D. Hui, Additive manufacturing (3D printing): A review of materials, methods, applications and challenges, Composites Part B: Engineering. 143 (2018) 172–196. https://doi.org/10.1016/j.compositesb.2018.02.012.

[3] A. Ambrosi, M. Pumera, 3D-printing technologies for electrochemical applications, Chem. Soc. Rev. 45 (2016) 2740–2755. https://doi.org/10.1039/C5CS00714C.

[4] X. Zhang, K. Guo, D. Shen, H. Feng, M. Wang, Y. Zhou, Y. Jia, Y. Liang, M. Zhou, Carbon black as an alternative cathode material for electrical energy recovery and transfer in a microbial battery, Sci Rep. 7 (2017) 6981. https://doi.org/10.1038/s41598-017-07174-z.

[5] M. Moalleminejad, D.D.L. Chung, Dielectric constant and electrical conductivity of carbon black as an electrically conductive additive in a manganese-dioxide electrochemical electrode, and their dependence on electrolyte permeation, Carbon. 91 (2015) 76–87. https://doi.org/10.1016/j.carbon.2015.04.047.

[6] Yu.V. Surovikin, Carbon Nanocomposites for Electrochemical Capacitors, Procedia Engineering. 113 (2015) 511–518. https://doi.org/10.1016/j.proeng.2015.07.344.

[7] P. Kossyrev, Carbon black supercapacitors employing thin electrodes, Journal of Power Sources. 201 (2012) 347–352. https://doi.org/10.1016/j.jpowsour.2011.10.106.

[8] J.-M. Kim, S.-W. Rhee, Electrochemical properties of porous carbon black layer as an electron injector into iodide redox couple, Electrochimica Acta. 83 (2012) 264–270. https://doi.org/10.1016/j.electacta.2012.07.107.

[9] J. Razumiene, J. Barkauskas, V. Kubilius, R. Meskys, V. Laurinavicius, Modified graphitized carbon black as transducing material for reagentless HO and enzyme sensors, Talanta. 67 (2005) 783–790. https://doi.org/10.1016/j.talanta.2005.04.004.

[10] C.W. Foster, M.P. Down, Y. Zhang, X. Ji, S.J. Rowley-Neale, G.C. Smith, P.J. Kelly, C.E. Banks, 3D Printed Graphene Based Energy Storage Devices, Sci Rep. 7 (2017) 42233. https://doi.org/10.1038/srep42233.

[11] F. Zhang, M. Wei, V.V. Viswanathan, B. Swart, Y. Shao, G. Wu, C. Zhou, 3D printing technologies for electrochemical energy storage, Nano Energy. 40 (2017) 418–431. https://doi.org/10.1016/j.nanoen.2017.08.037.

[12] P. Chang, H. Mei, S. Zhou, K.G. Dassios, L. Cheng, 3D printed electrochemical energy storage devices, J. Mater. Chem. A. 7 (2019) 4230–4258. https://doi.org/10.1039/C8TA11860D.

[13] L.-F. Chen, Y. Feng, H.-W. Liang, Z.-Y. Wu, S.-H. Yu, Macroscopic-Scale Three-Dimensional Carbon Nanofiber Architectures for Electrochemical Energy Storage Devices, Adv. Energy Mater. 7 (2017) 1700826. https://doi.org/10.1002/aenm.201700826.

[14] C.L. Manzanares Palenzuela, F. Novotný, P. Krupička, Z. Sofer, M. Pumera, 3D-Printed Graphene/Polylactic Acid Electrodes Promise High Sensitivity in Electroanalysis, Anal. Chem. 90 (2018) 5753–5757. https://doi.org/10.1021/acs.analchem.8b00083.

[15] C.W. Foster, H.M. Elbardisy, M.P. Down, E.M. Keefe, G.C. Smith, C.E. Banks, Additively manufactured graphitic electrochemical sensing platforms, Chemical Engineering Journal. 381 (2020) 122343. https://doi.org/10.1016/j.cej.2019.122343.

[16] Y. Zhai, Y. Yu, K. Zhou, Z. Yun, W. Huang, H. Liu, Q. Xia, K. Dai, G. Zheng, C. Liu, C. Shen, Flexible and wearable carbon black/thermoplastic polyurethane foam with a pinnate-veined aligned porous structure for multifunctional piezoresistive sensors, Chemical Engineering Journal. 382 (2020) 122985. https://doi.org/10.1016/j.cej.2019.122985.

[17] R.M. Cardoso, D.M.H. Mendonça, W.P. Silva, M.N.T. Silva, E. Nossol, R.A.B. da Silva, E.M. Richter, R.A.A. Muñoz, 3D printing for electroanalysis: From multiuse electrochemical cells to sensors, Analytica Chimica Acta. 1033 (2018) 49–57. https://doi.org/10.1016/j.aca.2018.06.021.

[18] A. Daneshkhah, S. Vij, A.P. Siegel, M. Agarwal, Polyetherimide/carbon black composite sensors demonstrate selective detection of medium-chain aldehydes including nonanal, Chemical Engineering Journal. 383 (2020) 123104. https://doi.org/10.1016/j.cej.2019.123104.

[19] R.M. Cardoso, S.V.F. Castro, M.N.T. Silva, A.P. Lima, M.H.P. Santana, E. Nossol, R.A.B. Silva, E.M. Richter, T.R.L.C. Paixão, R.A.A. Muñoz, 3D-printed flexible device combining sampling and detection of explosives, Sensors and Actuators B: Chemical. 292 (2019) 308–313. https://doi.org/10.1016/j.snb.2019.04.126.

[20] G.D. O'Neil, S. Ahmed, K. Halloran, J.N. Janusz, A. Rodríguez, I.M. Terrero Rodríguez, Single-step fabrication of electrochemical flow cells utilizing multi-material 3D printing, Electrochemistry Communications. 99 (2019) 56–60. https://doi.org/10.1016/j.elecom.2018.12.006.

[21] G.N. Meloni, 3D Printed and Microcontrolled: The One Hundred Dollars Scanning Electrochemical Microscope, Anal. Chem. 89 (2017) 8643–8649. https://doi.org/10.1021/acs.analchem.7b01764.

[22] Z. Rymansaib, P. Iravani, E. Emslie, M. Medvidović-Kosanović, M. Sak-Bosnar, R. Verdejo, F. Marken, All-Polystyrene 3D-Printed Electrochemical Device with Embedded Carbon Nanofiber-Graphite-Polystyrene Composite Conductor, Electroanalysis. 28 (2016) 1517–1523. https://doi.org/10.1002/elan.201600017.

[23] E. Vaněčková, M. Bouša, F. Vivaldi, M. Gál, J. Rathouský, V. Kolivoška, T. Sebechlebská, UV/VIS spectroelectrochemistry with 3D printed electrodes, Journal of Electroanalytical Chemistry. 857 (2020) 113760. https://doi.org/10.1016/j.jelechem.2019.113760.

[24] E. Vaněčková, M. Bouša, Š. Nováková Lachmanová, J. Rathouský, M. Gál, T. Sebechlebská, V. Kolivoška, 3D printed polylactic acid/carbon black electrodes with nearly ideal electrochemical behaviour, Journal of Electroanalytical Chemistry. 857 (2020) 113745. https://doi.org/10.1016/j.jelechem.2019.113745.

[25] C. Zhu, T. Liu, F. Qian, W. Chen, S. Chandrasekaran, B. Yao, Y. Song, E.B. Duoss, J.D. Kuntz, C.M. Spadaccini, M.A. Worsley, Y. Li, 3D printed functional nanomaterials for electrochemical energy storage, Nano Today. 15 (2017) 107–120. https://doi.org/10.1016/j.nantod.2017.06.007.

[26] Y. Wang, S. Su, L. Cai, B. Qiu, N. Wang, J. Xiong, C. Yang, X. Tao, Y. Chai, Monolithic Integration of All-in-One Supercapacitor for 3D Electronics, Adv. Energy Mater. 9 (2019) 1900037. https://doi.org/10.1002/aenm.201900037.

[27] R. Gusmão, M.P. Browne, Z. Sofer, M. Pumera, The capacitance and electron transfer of 3D-printed graphene electrodes are dramatically influenced by the type of solvent used for pre-treatment, Electrochemistry Communications. 102 (2019) 83–88. https://doi.org/10.1016/j.elecom.2019.04.004.

[28] S. Sato, D. Gondo, T. Wada, S. Kanehashi, K. Nagai, Effects of various liquid organic solvents on solvent-induced crystallization of amorphous poly(lactic acid) film, J. Appl. Polym. Sci. 129 (2013) 1607–1617. https://doi.org/10.1002/app.38833.

[29] P.L. dos Santos, V. Katic, H.C. Loureiro, M.F. dos Santos, D.P. dos Santos, A.L.B. Formiga, J.A. Bonacin, Enhanced performance of 3D printed graphene electrodes after electrochemical pre-treatment: Role of exposed graphene sheets, Sensors and Actuators B: Chemical. 281 (2019) 837–848. https://doi.org/10.1016/j.snb.2018.11.013.

[30] M.P. Browne, F. Novotný, Z. Sofer, M. Pumera, 3D Printed Graphene Electrodes' Electrochemical Activation, ACS Appl. Mater. Interfaces. 10 (2018) 40294–40301. https://doi.org/10.1021/acsami.8b14701.

[31] D.M. Wirth, M.J. Sheaff, J.V. Waldman, M.P. Symcox, H.D. Whitehead, J.D. Sharp, J.R. Doerfler, A.A. Lamar, G. LeBlanc, Electrolysis Activation of Fused-Filament-Fabrication 3D-Printed Electrodes for Electrochemical and Spectroelectrochemical Analysis, Anal. Chem. 91 (2019) 5553–5557. https://doi.org/10.1021/acs.analchem.9b01331.

[32] E. Vaněčková, M. Bouša, Š. Nováková Lachmanová, J. Rathouský, M. Gál, T. Sebechlebská, V. Kolivoška, 3D printed polylactic acid/carbon black electrodes with nearly ideal electrochemical behaviour, Journal of Electroanalytical Chemistry. 857 (2020) 113745. https://doi.org/10.1016/j.jelechem.2019.113745.

[33] E. Vaněčková, M. Bouša, R. Sokolová, P. Moreno-García, P. Broekmann, V. Shestivska, J. Rathouský, M. Gál, T. Sebechlebská, V. Kolivoška, Copper electroplating of 3D printed composite electrodes, Journal of Electroanalytical Chemistry. 858 (2020) 113763. https://doi.org/10.1016/j.jelechem.2019.113763.

[34] C.L. Manzanares-Palenzuela, S. Hermanova, Z. Sofer, M. Pumera, Proteinase-sculptured 3D-printed graphene/polylactic acid electrodes as potential biosensing platforms: towards enzymatic modeling of 3D-printed structures, Nanoscale. 11 (2019) 12124–12131. https://doi.org/10.1039/C9NR02754H.

[35] J.M. Kanczler, S.-H. Mirmalek-Sani, N.A. Hanley, A.L. Ivanov, J.J.A. Barry, C. Upton, K.M. Shakesheff, S.M. Howdle, E.N. Antonov, V.N. Bagratashvili, V.K. Popov, R.O.C. Oreffo, Biocompatibility and osteogenic potential of human fetal femur-derived cells on surface selective laser sintered scaffolds, Acta Biomaterialia. 5 (2009) 2063–2071. https://doi.org/10.1016/j.actbio.2009.03.010.

[36] K.T. Paula, G. Gaál, G.F.B. Almeida, M.B. Andrade, M.H.M. Facure, D.S. Correa, A. Riul, V. Rodrigues, C.R. Mendonça, Femtosecond laser micromachining of polylactic acid/graphene composites for designing interdigitated microelectrodes for sensor applications, Optics & Laser Technology. 101 (2018) 74–79. https://doi.org/10.1016/j.optlastec.2017.11.006.

[37] A.E. Ongaro, I. Keraite, A. Liga, G. Conoscenti, S. Coles, H. Schulze, T.T. Bachmann, K. Parvez, C. Casiraghi, N. Howarth, V. La Carubba, M. Kersaudy-Kerhoas, Laser Ablation of Poly(lactic acid) Sheets for the Rapid Prototyping of Sustainable, Single-Use, Disposable Medical Microcomponents, ACS Sustainable Chem. Eng. 6 (2018) 4899–4908. https://doi.org/10.1021/acssuschemeng.7b04348.

[38] L. Švorc, P. Tomčík, J. Svítková, M. Rievaj, D. Bustin, Voltammetric determination of caffeine in beverage samples on bare boron-doped diamond electrode, Food Chemistry. 135 (2012) 1198–1204. https://doi.org/10.1016/j.foodchem.2012.05.052.

[39] S.Y. Ly, Y.S. Jung, M.H. Kim, I. kwon Han, W.W. Jung, H.S. Kim, Determination of Caffeine Using a Simple Graphite Pencil Electrode with Square-Wave Anodic Stripping Voltammetry, Microchimica Acta. 146 (2004) 207–213. https://doi.org/10.1007/s00604-004-0209-3.

[40] L. Redivo, M. Stredanský, E. De Angelis, L. Navarini, M. Resmini, Ĺ. Švorc, Bare carbon electrodes as simple and efficient sensors for the quantification of caffeine in commercial beverages, R. Soc. Open Sci. 5 (2018) 172146. https://doi.org/10.1098/rsos.172146.

[41] D. Pantea, H. Darmstadt, S. Kaliaguine, C. Roy, Electrical conductivity of conductive carbon blacks: influence of surface chemistry and topology, Applied Surface Science. 217 (2003) 181–193. https://doi.org/10.1016/S0169-4332(03)00550-6.

[42] C.H. An Wong, A. Ambrosi, M. Pumera, Thermally reduced graphenes exhibiting a close relationship to amorphous carbon, Nanoscale. 4 (2012) 4972. https://doi.org/10.1039/c2nr30989k.

[43] P. Rizzarelli, G. Piredda, S. La Carta, E.F. Mirabella, G. Valenti, R. Bernet, G. Impallomeni, Characterization and laser-induced degradation of a medical grade polylactide, Polymer Degradation and Stability. 169 (2019) 108991. https://doi.org/10.1016/j.polymdegradstab.2019.108991.

[44] L. Chen, X. Zhang, Y. Wang, T.A. Osswald, Laser polishing of Cu/PLA composite parts fabricated by fused deposition modeling: Analysis of surface finish and mechanical properties, Polymer Composites. 41 (2020) 1356–1368. https://doi.org/10.1002/pc.25459.

[45] D.L. Sun, R.Y. Hong, J.Y. Liu, F. Wang, Y.F. Wang, Preparation of carbon nanomaterials using two-group arc discharge plasma, Chemical Engineering Journal. 303 (2016) 217–230. https://doi.org/10.1016/j.cej.2016.05.098.

[46] Y. Kameya, K. Hanamura, Kinetic and Raman spectroscopic study on catalytic characteristics of carbon blacks in methane decomposition, Chemical Engineering Journal. 173 (2011) 627–635. https://doi.org/10.1016/j.cej.2011.08.017.

[47] A.C. Ferrari, J.C. Meyer, V. Scardaci, C. Casiraghi, M. Lazzeri, F. Mauri, S. Piscanec, D. Jiang, K.S. Novoselov, S. Roth, A.K. Geim, Raman Spectrum of Graphene and Graphene Layers, Phys. Rev. Lett. 97 (2006) 187401. https://doi.org/10.1103/PhysRevLett.97.187401.

[48] M. Pawlyta, J.-N. Rouzaud, S. Duber, Raman microspectroscopy characterization of carbon blacks: Spectral analysis and structural information, Carbon. 84 (2015) 479–490. https://doi.org/10.1016/j.carbon.2014.12.030.

[49] W. Jia, Y. Luo, J. Yu, B. Liu, M. Hu, L. Chai, C. Wang, Effects of high-repetition-rate femtosecond laser micromachining on the physical and chemical properties of polylactide (PLA), Opt. Express. 23 (2015) 26932. https://doi.org/10.1364/OE.23.026932.

[50] J. Morikawa, A. Orie, T. Hashimoto, S. Juodkazis, Thermal diffusivity in femtosecond-laser-structured micro-volumes of polymers, Appl. Phys. A. 98 (2010) 551–556. https://doi.org/10.1007/s00339-009-5493-7.

[51] D. Qin, R.T. Kean, Crystallinity Determination of Polylactide by FT-Raman Spectrometry, Appl Spectrosc. 52 (1998) 488–495. https://doi.org/10.1366/0003702981943950.

[52] T.L. Barr, S. Seal, Nature of the use of adventitious carbon as a binding energy standard, Journal of Vacuum Science & Technology A: Vacuum, Surfaces, and Films. 13 (1995) 1239–1246. https://doi.org/10.1116/1.579868.

[53] F. Renò, D. D'Angelo, G. Gottardi, M. Rizzi, D. Aragno, G. Piacenza, F. Cartasegna, M. Biasizzo, F. Trotta, M. Cannas, Atmospheric Pressure Plasma Surface Modification of Poly(D,L-lactic acid) Increases Fibroblast, Osteoblast and Keratinocyte Adhesion and Proliferation, Plasma Processes Polym. 9 (2012) 491–502. https://doi.org/10.1002/ppap.201100139.

[54] P. Bertrand, L.T. Weng, Carbon Black Surface Characterization by TOF-SIMS and XPS, Rubber Chemistry and Technology. 72 (1999) 384–397. https://doi.org/10.5254/1.3538809.

[55] P. Niedziałkowski, T. Ossowski, P. Zięba, A. Cirocka, P. Rochowski, S.J. Pogorzelski, J. Ryl, M. Sobaszek, R. Bogdanowicz, Poly-l-lysine-modified boron-doped diamond electrodes for the amperometric detection of nucleic acid bases, Journal of Electroanalytical Chemistry. 756 (2015) 84–93. https://doi.org/10.1016/j.jelechem.2015.08.006.

[56] J. Wysocka, M. Cieslik, S. Krakowiak, J. Ryl, Carboxylic acids as efficient corrosion inhibitors of aluminium alloys in alkaline media, Electrochimica Acta. 289 (2018) 175–192. https://doi.org/10.1016/j.electacta.2018.08.070.

[57] M.P. Browne, V. Urbanova, J. Plutnar, F. Novotný, M. Pumera, Inherent impurities in 3D-printed electrodes are responsible for catalysis towards water splitting, J. Mater. Chem. A. 8 (2020) 1120–1126. https://doi.org/10.1039/C9TA11949C.

[58] Y.-J. Ko, K. Choi, S. Lee, J.-M. Cho, H.-J. Choi, S.W. Hong, J.-W. Choi, H. Mizuseki, W.-S. Lee, Chromate adsorption mechanism on nanodiamond-derived onion-like carbon, Journal of Hazardous Materials. 320 (2016) 368–375. https://doi.org/10.1016/j.jhazmat.2016.08.041.

[59] Y. Shao, G. Yin, J. Zhang, Y. Gao, Comparative investigation of the resistance to electrochemical oxidation of carbon black and carbon nanotubes in aqueous sulfuric acid solution, Electrochimica Acta. 51 (2006) 5853–5857. https://doi.org/10.1016/j.electacta.2006.03.021.

[60] H. Zhang, Y. Li, Y. Zhao, G. Li, F. Zhang, Carbon Black Oxidized by Air Calcination for Enhanced H_2O_2 Generation and Effective Organics Degradation, ACS Appl. Mater. Interfaces. 11 (2019) 27846–27853. https://doi.org/10.1021/acsami.9b07765.

[61] J.R. Harbour, M.J. Walzak, W. Limburg, J. Yanus, Generation of electron accepting surface sites in carbon blacks by peracetic acid oxidation, Carbon. 24 (1986) 725–729. https://doi.org/10.1016/0008-6223(86)90181-8.

[62] C.A. Frysz, D.D.L. Chung, Improving the electrochemical behavior of carbon black and carbon filaments by oxidation, Carbon. 35 (1997) 1111–1127. https://doi.org/10.1016/S0008-6223(97)00083-3.

[63] Y. Shao, G. Yin, J. Zhang, Y. Gao, Comparative investigation of the resistance to electrochemical oxidation of carbon black and carbon nanotubes in aqueous sulfuric acid solution, Electrochimica Acta. 51 (2006) 5853–5857. https://doi.org/10.1016/j.electacta.2006.03.021.

[64] P. Rochowski, M. Grzegorczyk, S. Pogorzelski, A wettability-based approach for the monitoring of drug transport through biological membranes, Journal of Colloid and Interface Science. 555 (2019) 352–360. https://doi.org/10.1016/j.jcis.2019.07.111.

[65] T. Swebocki, P. Niedziałkowski, A. Cirocka, E. Szczepańska, T. Ossowski, A. Wcisło, In pursuit of key features for constructing electrochemical biosensors – electrochemical and acid-base characteristic of self-assembled monolayers on gold, Supramolecular Chemistry. 32 (2020) 256–266. https://doi.org/10.1080/10610278.2020.1739685.

[66] K.-Y. Law, Definitions for Hydrophilicity, Hydrophobicity, and Superhydrophobicity: Getting the Basics Right, J. Phys. Chem. Lett. 5 (2014) 686–688. https://doi.org/10.1021/jz402762h.

[67] A. Orue, A. Eceiza, C. Peña-Rodriguez, A. Arbelaiz, Water Uptake Behavior and Young Modulus Prediction of Composites Based on Treated Sisal Fibers and Poly(Lactic Acid), Materials. 9 (2016) 400. https://doi.org/10.3390/ma9050400.

[68] A.M. Pinto, S. Moreira, I.C. Gonçalves, F.M. Gama, A.M. Mendes, F.D. Magalhães, Biocompatibility of poly(lactic acid) with incorporated graphene-based materials, Colloids and Surfaces B: Biointerfaces. 104 (2013) 229–238. https://doi.org/10.1016/j.colsurfb.2012.12.006.

[69] R.E. Przekop, M. Kujawa, W. Pawlak, M. Dobrosielska, B. Sztorch, W. Wieleba, Graphite Modified Polylactide (PLA) for 3D Printed (FDM/FFF) Sliding Elements, Polymers. 12 (2020) 1250. https://doi.org/10.3390/polym12061250.

[70] X. Lu, B. Kang, S. Shi, Selective Localization of Carbon Black in Bio-Based Poly (Lactic Acid)/Recycled High-Density Polyethylene Co-Continuous Blends to Design Electrical Conductive Composites with a Low Percolation Threshold, Polymers. 11 (2019) 1583. https://doi.org/10.3390/polym11101583.

[71] L.E.C. de Torre, E.J. Bottani, A. Martínez-Alonso, A. Cuesta, A.B. García, J.M.D. Tascón, Effects of oxygen plasma treatment on the surface of graphitized carbon black, Carbon. 36 (1998) 277–282. https://doi.org/10.1016/S0008-6223(97)00180-2.

[72] S.M. Jaseem, N.A. Ali, Antistatic packaging of carbon black on plastizers biodegradable polylactic acid nanocomposites, J. Phys.: Conf. Ser. 1279 (2019) 012046. https://doi.org/10.1088/1742-6596/1279/1/012046.

[73] B.C. Lourenção, R.A. Medeiros, R.C. Rocha-Filho, O. Fatibello-Filho, Simultaneous Differential Pulse Voltammetric Determination of Ascorbic Acid and Caffeine in Pharmaceutical Formulations Using a

Boron-Doped Diamond Electrode, Electroanalysis. 22 (2010) 1717–1723. https://doi.org/10.1002/elan.200900612.

[74] BarbaraH. Hansen, G. Dryhurst, Electrochemical oxidation of theobromine and caffeine at the pyrolytic graphite electrode, Journal of Electroanalytical Chemistry and Interfacial Electrochemistry. 30 (1971) 407–416. https://doi.org/10.1016/0368-1874(71)87024-7.

[75] M.A. Raj, S.A. John, Simultaneous determination of uric acid, xanthine, hypoxanthine and caffeine in human blood serum and urine samples using electrochemically reduced graphene oxide modified electrode, Analytica Chimica Acta. 771 (2013) 14–20. https://doi.org/10.1016/j.aca.2013.02.017.

[76] N. Spataru, S. Bulusu, D. Tryk, A. Fujishima, Anodic Voltammetry of Xanthine, Theophylline, Theobromine and Caffeine at Conductive Diamond Electrodes and Its Analytical Application, Electroanalysis. 14 (2002) 721–728. https://doi.org/10.1002/1521-4109(200206)14:11<721::AID-ELAN721>3.0.CO;2-1.

[77] T.T. Minh, N.H. Phong, H. Van Duc, D.Q. Khieu, Microwave synthesis and voltammetric simultaneous determination of paracetamol and caffeine using an MOF-199-based electrode, J Mater Sci. 53 (2018) 2453–2471. https://doi.org/10.1007/s10853-017-1715-0.

[78] B. Mekassa, M. Tessema, B.S. Chandravanshi, Simultaneous determination of caffeine and theophylline using square wave voltammetry at poly(1 -aspartic acid)/functionalized multi-walled carbon nanotubes composite modified electrode, Sensing and Bio-Sensing Research. 16 (2017) 46–54. https://doi.org/10.1016/j.sbsr.2017.11.002.

[79] M.P. Browne, F. Novotný, Z. Sofer, M. Pumera, 3D Printed Graphene Electrodes' Electrochemical Activation, ACS Appl. Mater. Interfaces. 10 (2018) 40294–40301. https://doi.org/10.1021/acsami.8b14701.

[80] E.M. Richter, D.P. Rocha, R.M. Cardoso, E.M. Keefe, C.W. Foster, R.A.A. Munoz, C.E. Banks, Complete Additively Manufactured (3D-Printed) Electrochemical Sensing Platform, Anal. Chem. 91 (2019) 12844–12851. https://doi.org/10.1021/acs.analchem.9b02573.

[81] B. Brunetti, E. Desimoni, P. Casati, Determination of Caffeine at a Nafion-Covered Glassy Carbon Electrode, Electroanalysis. 19 (2007) 385–388. https://doi.org/10.1002/elan.200603679.

[82] M. Tefera, A. Geto, M. Tessema, S. Admassie, Simultaneous determination of caffeine and paracetamol by square wave voltammetry at poly(4-amino-3-hydroxynaphthalene sulfonic acid)-modified glassy carbon electrode, Food Chemistry. 210 (2016) 156–162. https://doi.org/10.1016/j.foodchem.2016.04.106.

[83] X.-Q. Xiong, K.-J. Huang, C.-X. Xu, C.-X. Jin, Q.-G. Zhai, Glassy carbon electrode modified with poly(taurine)/TiO2-graphene composite film for determination of acetaminophen and caffeine, CI&CEQ. 19 (2013) 359–368. https://doi.org/10.2298/CICEQ120325070X.

[84] Y. Gao, H. Wang, L. Guo, Simultaneous determination of theophylline and caffeine by large mesoporous carbon/Nafion modified electrode, Journal of Electroanalytical Chemistry. 706 (2013) 7–12. https://doi.org/10.1016/j.jelechem.2013.07.030.

Supplementary Information

Helium-assisted, solvent-free electro-activation of 3D printed conductive carbon-polylactide electrodes by pulsed laser ablation

Maciej J. Glowacki[1,#], Mateusz Cieslik[1,#], Miroslaw Sawczak[2], Adrian Koterwa[3],

Iwona Kaczmarzyk[1], Rafal Jendrzejewski[2], Lukasz Szynkiewicz[1], Tadeusz Ossowski[3],

Robert Bogdanowicz[1], Pawel Niedzialkowski[3], Jacek Ryl[1,*]

[1] Gdansk University of Technology, Narutowicza 11/12, 80-233 Gdansk, Poland

[2] The Szewalski Institute of Fluid-Flow Machinery, Polish Academy of Sciences, Fiszera 14, 80-231 Gdansk, Poland

[3] Department of Analytical Chemistry, University of Gdansk, Wita Stwosza 63, Gdansk 80-308, Poland
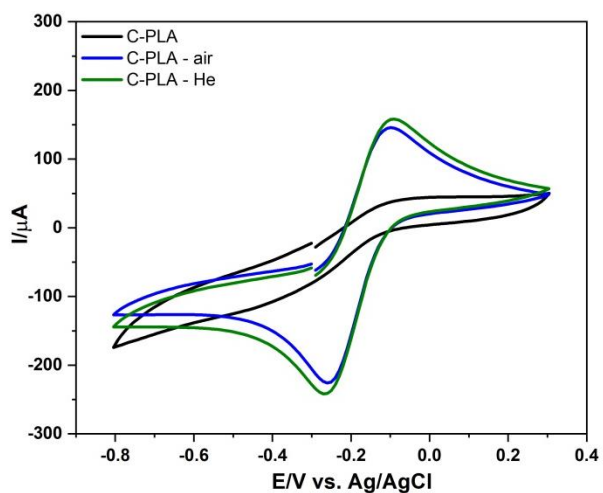
* Correspondence: Jacek Ryl – jacek.ryl@pg.edu.pl

[#] these authors contributed equally to the manuscript

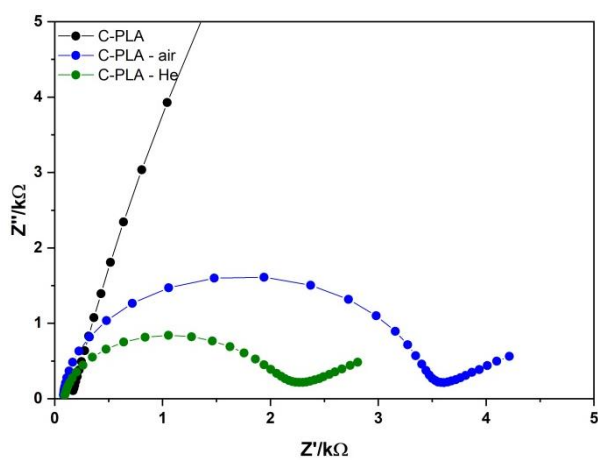## S1. Thermogravimetric analysis of the ProtoPasta CB-PLA filament
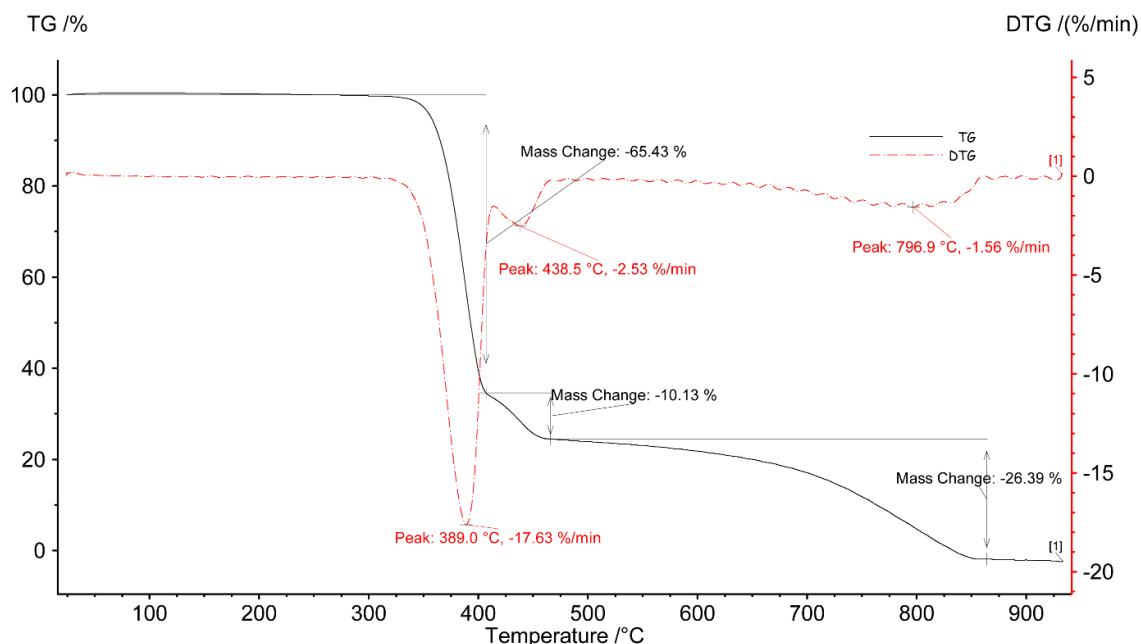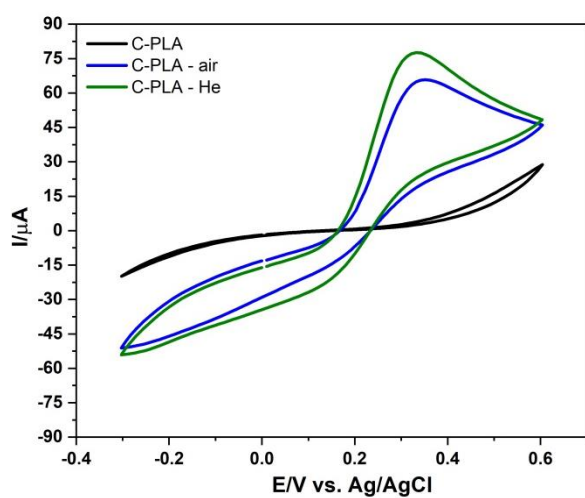

S2. CV and EIS measurements of CB-PLA surface activation by laser ablation, studied with various redox active species
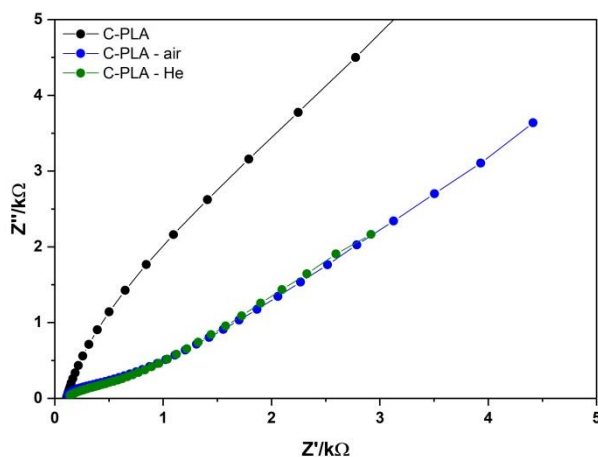
(i) $[Ru(NH_3)_6]^{2+/3+}$
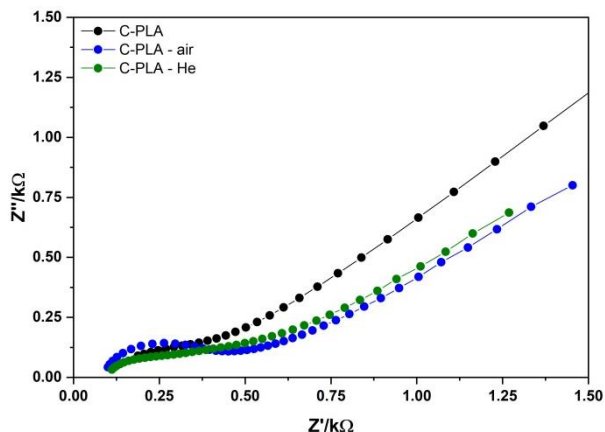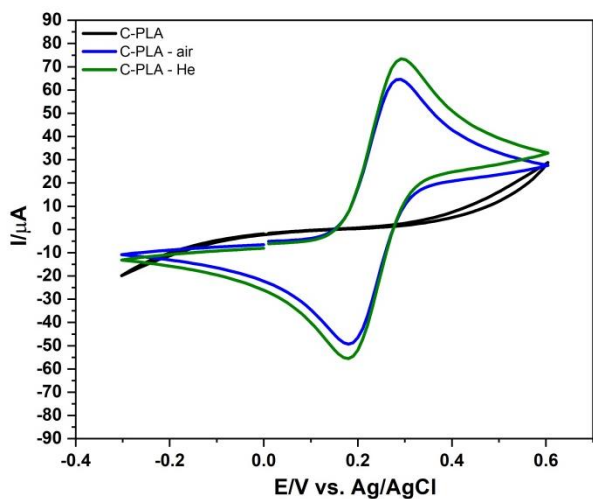
(ii) $[Fe(CN)_6]^{3-/4-}$

(iii) $FcDM^{0/+}$ (FcDM = 1,1′-ferrocenedimethanol)

S3. $[Ru(NH_3)_6]^{2+/3+}$ redox process on laser ablated conductive PLA surface

Activation method	Method clarification	Material	k^0_{obs}	Reference
Electrochemical pre-treatment	1) anodic polarization (+1.8V) 2) cathodic polarization (-1.8V) / 0.1M PBS	Black Magic 3D	1) 7.64×10^{-4} 2) 4.72×10^{-4}	[S1]
Not activated	-	Black Magic 3D	4.58×10^{-4}	[S2]
1) Electrochemical pre-treatment 2) Mechanical polishing 3) Chemical pre-treatment	1) anodic polarization (+1.8V) / 0.1M PBS 2) Alumina polishing 3) DMF immersion (10min) 4) NaOH immersion (30min) 5) HNO$_3$ immersion (60min) 6) H$_2$SO$_4$ immersion (60min)	Black Magic 3D	1) 1.53×10^{-3} 2) 1.20×10^{-4} 3) 3.85×10^{-4} 4) 9.34×10^{-4} 5) 1.53×10^{-4} 6) 3.25×10^{-4}	[S3]
Electrochemical pre-treatment	10 V applied potential for 10s	PLA-CNT	1.46×10^{-4}	[S4]
Electrochemical pre-treatment	6V applied potential for 10s	PLA-CNT	1.24×10^{-4}	[S5]
Polishing and electrochemical pre-treatment	anodic (+1.4V) and cathodic (-1.0V)/ 0.5M NaOH	Proto-pasta	9.9×10^{-3}	[S6]

In regard to the use of different activation methods for improving electrochemical response, DMF solvent activation and NaOH treatment combined with electrochemical activation promoted an increase in the electrochemical response, electron transfer rate. Both electrodes showed faradic processes for the $[Ru(NH_3)]_6^{2+/3+}$ redox reaction, the peak-to-peak separation are comparable to our measurement data of the novel activated method with laser ablation. The electrochemical activation treatments present comparable or slightly worse heterogeneous rate constant value. Moreover, the EIS spectra presented in section S2 of the Supporting Information file reveal the charge transfer resistance of approx. 230 and 300 Ohm for He- and air-atmosphere ablated samples, respectively, which is

comparable to the charge transfer resistance of G-PLA electrodes after chemical treatment followed by electrochemical activation shown by Kalinke et al. [S3].

References:

[S1] P.L. dos Santos, V. Katic, H.C. Loureiro, M.F. dos Santos, D.P. dos Santos, A.L.B. Formiga, J.A. Bonacin, Enhanced performance of 3D printed graphene electrodes after electrochemical pre-treatment: Role of exposed graphene sheets, Sensors and Actuators B: Chemical. 281 (2019) 837–848. https://doi.org/10.1016/j.snb.2018.11.013.

[S2] P. Chang, H. Mei, S. Zhou, K.G. Dassios, L. Cheng, 3D printed electrochemical energy storage devices, J. Mater. Chem. A. 7 (2019) 4230–4258. https://doi.org/10.1039/C8TA11860D.

[S3] C. Kalinke, N.V. Neumsteir, G. de O. Aparecido, T.V. de B. Ferraz, P.L. dos Santos, B.C. Janegitz, J.A. Bonacin, Comparison of activation processes for 3D printed PLA-graphene electrodes: electrochemical properties and application for sensing of dopamine, Analyst. 145 (2020) 1207–1218. https://doi.org/10.1039/C9AN01926J.

[S4] E. Vaněčková, M. Bouša, Š. Nováková Lachmanová, J. Rathouský, M. Gál, T. Sebechlebská, V. Kolivoška, 3D printed polylactic acid/carbon black electrodes with nearly ideal electrochemical behaviour, Journal of Electroanalytical Chemistry. 857 (2020) 113745. https://doi.org/10.1016/j.jelechem.2019.113745.

[S5] E. Vaněčková, M. Bouša, F. Vivaldi, M. Gál, J. Rathouský, V. Kolivoška, T. Sebechlebská, UV/VIS spectroelectrochemistry with 3D printed electrodes, Journal of Electroanalytical Chemistry. 857 (2020) 113760. https://doi.org/10.1016/j.jelechem.2019.113760.

[S6] E.M. Richter, D.P. Rocha, R.M. Cardoso, E.M. Keefe, C.W. Foster, R.A.A. Munoz, C.E. Banks, Complete Additively Manufactured (3D-Printed) Electrochemical Sensing Platform, Anal. Chem. 91 (2019) 12844–12851. https://doi.org/10.1021/acs.analchem.9b02573.

S4. Caffeine electro-oxidation mechanism
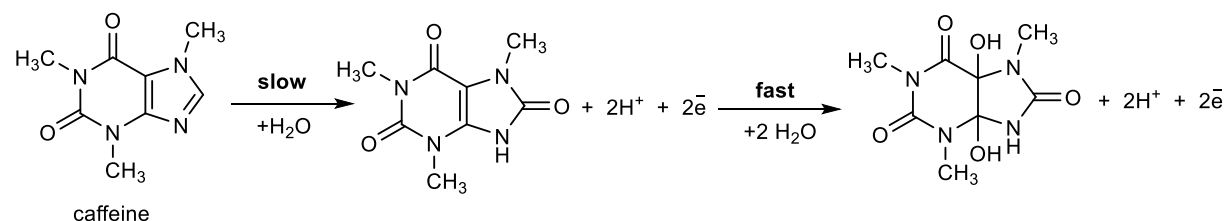
caffeine

References:

[S7] B.C. Lourenção, R.A. Medeiros, R.C. Rocha-Filho, O. Fatibello-Filho, Simultaneous Differential Pulse Voltammetric Determination of Ascorbic Acid and Caffeine in Pharmaceutical Formulations Using a Boron-Doped Diamond Electrode, Electroanalysis. 22 (2010) 1717–1723. https://doi.org/10.1002/elan.200900612.

[S8] BarbaraH. Hansen, G. Dryhurst, Electrochemical oxidation of theobromine and caffeine at the pyrolytic graphite electrode, Journal of Electroanalytical Chemistry and Interfacial Electrochemistry. 30 (1971) 407–416. https://doi.org/10.1016/0368-1874(71)87024-7.